

# Field-induced modulation of the conductance, thermoelectric power, and magnetization in ballistic coupled double quantum wires under a tilted magnetic field

Danhong Huang

*Air Force Research Laboratory, Space Vehicles Directorate, Kirtland Air Force Base, New Mexico 87117, USA*

S. K. Lyo

*Sandia National Laboratories, Albuquerque, New Mexico 87185, USA*

K. J. Thomas and M. Pepper

*Cavendish Laboratory, University of Cambridge, Madingley Road, Cambridge CB3 0HE, United Kingdom*

(Received 21 September 2007; revised manuscript received 17 December 2007; published 26 February 2008)

The effect of a tilted magnetic field  $B$  on the modulation of tunneling, the ballistic conductance, the ballistic electron-diffusion thermoelectric power, and the orbital magnetization is studied for tunnel-coupled ballistic double quantum wires. The magnetic field has a component  $B_y$  along the wires and a component  $B_x$  perpendicular to the plane that contains both wires. We find that  $B_y$  alters the  $B_x$  dependence of the electronic and transport properties drastically in the presence of interwire tunneling. The latter has been studied extensively in the literatures in the absence of  $B_y$  and is known to show many interesting transport properties. The presence of  $B_y$  causes the effective tunneling integral to oscillate continuously with sign changes and decay eventually for large  $B_y$ . The  $B_y$ -induced interwire tunnel coupling between different sublevels and the quenching of it under a large  $B_y$  were both observed experimentally by Thomas *et al.* [Phys. Rev. B **59**, 12252 (1999)].

DOI: [10.1103/PhysRevB.77.085320](https://doi.org/10.1103/PhysRevB.77.085320)

PACS number(s): 72.20.My, 73.40.Gk, 72.20.Fr, 73.40.Kp

## I. INTRODUCTION

Long high-mobility semiconductor quantum wires (QWRs) ( $\geq 20 \mu\text{m}$ ) are now within reach. For QWRs with lengths comparable to the mean free path but shorter than the localization length, it is not always clear if they are in the ballistic or diffusive regime due to the uncertainties in the mean free paths and frequent ambiguous features of the conductance steps. It was shown previously that the field dependence of the quantized conductance and the thermoelectric power (TEP) of QWRs with the magnetic field ( $B$ ) applied in the perpendicular direction exhibits drastically different behaviors for the diffusive and ballistic regimes.<sup>1-5</sup> Moreover, the transport properties of the double quantum wires (DQWRs) under a magnetic field ( $B_x$ ) perpendicular to the plane containing the wires were quite different from those of single quantum wires (SQWRs).<sup>1,6-12</sup> The purpose of this paper is to show that the presence of an additional component of the magnetic field  $B_y$  along the wires alters many previously known interesting  $B_x$  dependence of transport and electronic properties sensitively.

Coupled DQWRs to be studied in this paper are stacked in the  $z$  direction, as shown in Fig. 1. The transverse confinement in the  $x$  direction is assumed to be parabolic with the sublevels labeled by  $n=0, 1, 2, \dots$ . The channel constrictions in the  $x$  direction are achieved independently through top and bottom split gates, which allow probing the 2D-2D, 2D-1D, and 1D-1D regimes by adjusting the gate biases.<sup>13,14</sup> The quantum wires extend in the  $y$  direction and are separated by a thin barrier layer allowing interwell electron tunneling in the  $z$  direction. A current flows in the  $y$  direction between the source and drain contacts. A magnetic field  $\mathbf{B}=(B_x, B_y, 0)$  is applied within the  $xy$  plane perpendicular to the growth ( $z$ ) direction.

For the diffusive conductance  $G$ , a number of recent studies focused mainly on the effects of elastic scattering by impurities and interface roughness.<sup>1,6-12</sup> Very recently, we assessed the relative contributions from electron-phonon<sup>3</sup> and electron-electron<sup>5</sup> scattering and found that they were significant even at relatively low temperatures and densities in multisublevel structures. In these scattering systems, inter-sublevel electron-phonon and electron-electron scattering are responsible, respectively, for the momentum-relaxation and the energy-relaxation processes. We developed a formalism

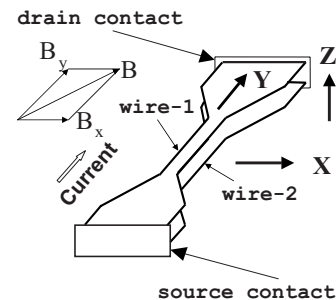


FIG. 1. A schematic illustration of the tunnel-coupled double quantum wires stacked in the  $z$  (growth) direction. The two narrow GaAs conducting channels confined in the  $x$  direction are formed by applying a negative voltage to two metallic split gates with respect to the grounded back gate (not shown). The formed quantum wires extend in the  $y$  direction. There exists a thin AlGaAs barrier layer between the two wells in the  $z$  direction, which allows the electron tunneling between two wires. The linear electron density in the wires can be varied by applying a negative voltage to a depletion gate (not shown) on the surface of double quantum wells. A magnetic field  $\mathbf{B}=(B_x, B_y, 0)$  is applied to the system within the  $xy$  plane perpendicular to the growth direction. A current flows along the wires between the source and drain contacts.

which yielded diffusive  $G$  and TEP to a desired accuracy for a general quasi-one-dimensional (1D) electronic structure and obtained the numerical results from this formalism.<sup>2,3,5</sup>

Ballistic transport properties of quasi-1D  $n$ -doped semiconductor structures, on the other hand, are of particular interest for a variety of novel physical phenomena and possible new device applications. The earliest realization of SQWRs is the quantum point contact in which the channel length is very short, of the order of a fraction of a micrometer. The measured conductance  $G$  is quantized and decreases in steps of  $2e^2/h$  in a spin-degenerate system, when the channel width is gradually reduced,<sup>15</sup> with  $e$  and  $h$  being the absolute electronic charge and Planck's constant, respectively. Similar quantized  $G$  steps are also observed in both SQWRs and DQWRs as a function of  $B$  applied in the growth ( $z$ ) direction perpendicular to the wires.<sup>16,17</sup> Recently, ballistic electron-diffusion TEP,  $S_d$ , was observed in SQWRs<sup>18</sup> and studied theoretically at zero  $B$ .<sup>18–20</sup> Previous studies of  $S_d$  are relevant to simple band structures with a single minimum for each sublevel.<sup>18–20</sup> Quantized TEP was studied recently for complicated band structures with two minima and one maximum for each sublevel in tunnel-coupled DQWRs in the presence of a perpendicular magnetic field in the  $x$  direction.<sup>4,21,22</sup>

For a two-dimensional electron gas (2DEG) in a single quantum well (QW), the quantization of electron kinetic energy into Landau levels occurs in the presence of a strong  $B$  in the  $z$  direction perpendicular to the layer. For this 2DEG system, important information about the structure of the energy spectrum can be extracted from measurements of thermodynamic quantities<sup>23–27</sup> such as the entropy, the heat capacity, and the orbital magnetization at finite temperatures. Self-consistent theories<sup>28,29</sup> were used to explain these thermodynamic measurements. Recently, effects of a tilted (in the  $xz$  plane)  $B$  on the orbital magnetization were studied for both single 2D QWs<sup>30</sup> (in the  $xy$  plane) and SQWRs<sup>31</sup> (extended in the  $y$  direction). For the latter, jumping and oscillating orbital magnetizations were found for  $B$  applied, respectively, in the  $z$  and  $x$  directions due to coupling of two orthogonal harmonic oscillators.

When  $B$  is applied in the  $x$  direction perpendicular to tunnel-coupled DQWRs, the  $B$  dependences of both the quantized magnetoconductance<sup>32</sup> and the ballistic electron-diffusion thermoelectric power<sup>4</sup> were extensively studied. In this paper, we generalize our previous results<sup>4,32</sup> for ballistic electron transport in DQWRs to include the effects of inter-wire electron tunneling between  $n \neq n'$  transverse sublevels, as well as the resulting  $B$  dependence of ballistic conductance, ballistic electron-diffusion thermoelectric power, and orbital magnetization, with  $B$  applied in an arbitrary orientation within the  $xy$  plane. For a tilted magnetic field, the quantum transport in diffusive wires has not yet been studied theoretically. However, some experimental<sup>33</sup> and theoretical (in a perturbative approach)<sup>34</sup> studies for the effect of a tilted magnetic field on the quantum transport in ballistic wires were reported. In this paper, we limit ourselves only to the case of ballistic transport.

The outline of this paper is as follows. In Sec. II, we present expressions for the ballistic conductance, the ballistic electron-diffusion thermoelectric power, and the orbital mag-

netization in tunnel-coupled DQWRs under  $B$  within the  $xy$  plane in an arbitrary orientation. In Sec. III, we discuss numerical results for the effect of a tilted  $B$  field on the inter-wire tunnel coupling, sublevel repulsion, the ballistic conductance, the ballistic electron-diffusion thermoelectric power, and the orbital magnetization. A brief conclusion and a remark are given in Sec. IV.

## II. MODEL AND THEORY

For  $\mathbf{B}$  in the  $xy$  plane, the corresponding vector potential in the Landau gauge is written as  $\mathbf{A}=(B_y z, -B_x z, 0)$ . As a result, the Hamiltonian of the system in Fig. 1 takes the form

$$\mathcal{H} = \frac{\hbar^2}{2m^*} \left( k - \frac{z}{\ell_{cx}^2} \right)^2 + \frac{\hbar^2}{2m^*} \left( -i \frac{\partial}{\partial x} + \frac{z}{\ell_{cy}^2} \right)^2 + \frac{1}{2} m^* \omega_x^2 x^2 - \frac{\hbar^2}{2m^*} \frac{\partial^2}{\partial z^2} + V_{\text{DQW}}(z), \quad (1)$$

where  $V_{\text{DQW}}(z)$  is a rectangular potential profile of the symmetric double quantum wells in the  $z$  direction,  $\ell_{cx} = (\hbar/eB_x)^{1/2}$  and  $\ell_{cy} = (\hbar/eB_y)^{1/2}$  are the magnetic lengths in the  $x$  and  $y$  directions,  $m^*$  is the effective mass of electrons,  $k$  is the wave number in the wire ( $y$ ) direction, and  $\hbar\omega_x$  is the uniform transverse-sublevel separation at  $B=0$ . In this paper, we limit ourselves to the case where the thickness of the wires in the  $z$  direction is so thin that only the ground tunnel-split doublet is occupied.<sup>35</sup> At the same time, the width of the wires in the  $x$  direction is large enough to allow occupation of multiple transverse sublevels.<sup>36</sup>

For the occupied ground doublet, electrons are strongly confined in the  $z$  direction and the interwell electron tunneling is weak. Therefore, a tight-binding model is adequate to describe electron tunneling between the wires.<sup>35</sup> When a tight-binding model is employed, we can equivalently regard the wires with finite thickness in the  $z$  direction as separated strips (zero thickness) containing freely moving electrons along the strips and residing at  $z_1$  and  $z_2$  with the distance  $d=|z_1-z_2|$  between them. Consequently, we find from Eq. (1) that  $\mathcal{H}=\mathcal{H}_x+\mathcal{H}_z$  for these two strips at  $z_i$  ( $i=1,2$ ) with

$$\mathcal{H}_x = \frac{\hbar^2}{2m^*} \left( k - \frac{z_i}{\ell_{cx}^2} \right)^2 + \frac{\hbar^2}{2m^*} \left( -i \frac{\partial}{\partial x} + \frac{z_i}{\ell_{cy}^2} \right)^2 + \frac{1}{2} m^* \omega_x^2 x^2, \quad (2)$$

$$\mathcal{H}_z = -\frac{\hbar^2}{2m^*} \frac{\partial^2}{\partial z^2} + V_{\text{DQW}}(z). \quad (3)$$

By introducing a Fourier transform to the wave function  $\xi(x)$  in the  $x$  direction,

$$\xi(x) = \frac{1}{\sqrt{2\pi}} \int_{-\infty}^{\infty} dq \phi(q) e^{iqx}, \quad (4)$$

we rewrite the Hamiltonian  $\mathcal{H}_x$  in Eq. (2) in the  $q$  space as

$$\mathcal{H}_x = \frac{\hbar^2}{2m^*} \left( k - \frac{z_i}{\ell_{cx}^2} \right)^2 + \frac{1}{2} m^* \omega_x^2 \left( s + \frac{z_i \ell_x^2}{\ell_{cy}^2} \right)^2 - \frac{\hbar^2}{2m^*} \frac{\partial^2}{\partial s^2}, \quad (5)$$

where  $s = \ell_x^2 q$  and  $\ell_x = \sqrt{\hbar/m^* \omega_x}$  represents the harmonic confinement width of electrons in the  $x$  direction. The electron sublevels in the  $x$  direction are obtained from the Schrödinger equation associated with the Fourier transformed Hamiltonian in Eq. (5),

$$E_n^x(k) = \frac{\hbar^2}{2m^*} \left( k - \frac{z_i}{\ell_{cx}^2} \right)^2 + \left( n + \frac{1}{2} \right) \hbar \omega_x, \quad (6)$$

with  $n=0, 1, 2, \dots$  for two wires at  $z_1$  and  $z_2$ . The normalized electron wave function in the  $xy$  plane for each wire is given by

$$\begin{aligned} \Psi_{kn}^i(x, y) &= \frac{1}{\sqrt{L_y}} e^{iky} \frac{\ell_x}{\sqrt{2\pi}} \int_{-\infty}^{\infty} dq e^{iqx} \phi_n \left[ \left( q + \frac{z_i}{\ell_{cy}^2} \right) \ell_x^2 \right] \\ &= \frac{1}{\sqrt{L_y}} e^{iky} e^{in\pi/2} e^{-iz_i x / \ell_{cy}^2} \phi_n(x), \end{aligned} \quad (7)$$

where  $\Psi_{kn}^i(x, y)$  acquires a phase factor  $\exp(-iz_i x / \ell_{cy}^2)$  depending on the wire position,  $L_y$  is the length of the wires, and

$$\phi_n(x) = \sqrt{\frac{1}{2^n n! \pi^{1/2} \ell_x}} e^{-x^2/2\ell_x^2} H_n \left( \frac{x}{\ell_x} \right), \quad (8)$$

is the harmonic-oscillator wave function with  $H_n(x)$  being the  $n$ th-order Hermit polynomial. In Eq. (6),  $E_n^x(k)$  is independent of  $B_y$  and the effect of  $B_x$  is to displace the two groups of parabolas of different wires with each other in  $k$  space.<sup>36</sup> However, the relative phase difference of the  $xy$  plane wave functions in Eq. (7) between the two wires is proportional to  $B_y$ . This introduces nonvanishing tunnel coupling between  $n \neq n'$  transverse sublevels, as seen from the Hamiltonian matrix  $[\mathcal{H}_{j,j'}]$  given below. For each  $k$  value, the total electron energy  $E_j(k)$  is determined by the eigenvalue equation, i.e.,  $\det[\mathcal{H}_{j,j'} - E_j(k) \delta_{j,j'}] = 0$ . The Hamiltonian matrix elements introduced in this equation are independent of  $k$  and given by an effective tunneling integral in the tight-binding approximation

$$\mathcal{H}_{j,j'} = \frac{1}{2} \Delta_{\text{SAS}} \sqrt{\frac{n_{<}!}{2^m n_{>}!}} \phi_B^m e^{-\phi_B^2/4} L_{n_{<}}^{(m)} \left( \frac{\phi_B^2}{2} \right), \quad (9)$$

where  $j$  and  $j'$  refer to the quantum states  $n$  and  $n'$  in different wires. The result in Eq. (9) is the product of the interwell interaction integral ( $\Delta_{\text{SAS}}/2$ ) in the  $z$  direction and the overlap integral of the wave functions in the  $xy$  plane. The Hamiltonian matrix  $[\mathcal{H}_{j,j'}]$  becomes diagonal when  $j$  and  $j'$  belong to the quantum states in the same quantum wire with its diagonal elements being the eigenenergy given by  $E_n^x(k)$  in Eq. (6) for a single quantum wire. Here,  $L_n^{(m)}(x)$  is the  $n$ th-order associated Laguerre polynomial and the indices  $j$  and  $j'$  are related to the transverse-sublevel indices  $n$  and  $n'$  of the two quantum wires with  $n, n' \in [0, N_t - 1]$ . We label the index  $j \in [1, N_t]$  and  $j \in [N_t + 1, 2N_t]$ , respectively, for the

upper and lower wires with  $N_t$  being the total number of transverse sublevels considered in our calculations for each wire. Moreover,  $\phi_B = d\ell_x / \ell_{cy}^2$  is the number of magnetic-flux quanta through the cross section  $d\ell_x$  spanned by two wires in the  $xz$  plane and  $\Delta_{\text{SAS}}$  is the ground-state tunnel splitting at  $B=0$ . We have defined in Eq. (9) the notations for the integers  $n_{<} = \min(n, n')$ ,  $n_{>} = \max(n, n')$ , and  $m = n_{>} - n_{<}$ . For  $B_y=0$ , Eq. (9) is  $\mathcal{H}_{j,j'} = \delta_{m,0} \Delta_{\text{SAS}}/2$ , indicating interwire tunnel coupling only between  $n=n'$  transverse sublevels in the two wires. However, different sublevels ( $m \neq 0$ ) become tunnel coupled for  $B_y \neq 0$ . When  $\phi_B^2/2$  is one of the roots of  $L_n^{(m)}(x)$  at a certain value of  $B_y$ , either the intrasublevel ( $m=0$ ) or the intersublevel ( $m \neq 0$ ) tunnel coupling vanishes. The Lorentz force along the wires due to  $B_x$  and the tunneling motion introduces a relative displacement  $\Delta k = deB_x/\hbar$  in  $k$  space. On the other hand, the transverse Lorentz force due to  $B_y$  and the tunneling motion provides a momentum shift  $\hbar \Delta q \equiv -deB_y = -\hbar \phi_B / \ell_x$  for the Fourier component  $q$  in Eq. (4) between the initial and final tunneling states, giving rise to a tunneling modulation for medium values  $\phi_B$  and a quenching of tunneling for  $\phi_B^2/4 \gg 1$ .

The quantized magnetoconductance  $G$  in the spin-degenerate quasi-1D Fermi liquid at finite temperature  $T$  is determined by the total number of pairs of Fermi points  $N_F(E)$  at electron energy  $E$  and given by<sup>1</sup>

$$G(B_x, B_y) = \frac{2e^2}{h} \int_0^\infty dE [-f'_0(E)] N_F(E) \equiv \frac{2e^2}{h} \mathcal{N}(\mu_c), \quad (10)$$

where  $f_0(E)$  is the Fermi function and  $f'_0(E)$  is the first derivative of  $f_0(E)$  with respect to  $E$ . For a fixed electron energy  $E$ ,  $N_F(E)$  in Eq. (10) depends on  $\mathbf{B}$ . From Eq. (10), it is clear that  $G(B_x, B_y)$  depends on the orientation of  $\mathbf{B}$  in addition to its magnitude dependence.

The ballistic electron-diffusion thermoelectric power  $S_d$  is defined as the ratio of the heat current to the charge current of electrons divided by  $T$  under a bias. For symmetric electronic structures, it is given by<sup>4,37</sup>

$$\begin{aligned} S_d(B_x, B_y) &= -\frac{k_B}{eF} \sum_{j,\gamma} C_{j,\gamma} [\beta [E_j(k_\gamma) - \mu_c(T)] f_0[E_j(k_\gamma)] \\ &\quad + \ln\{1 + \exp[\beta(\mu_c(T) - E_j(k_\gamma))]\}], \end{aligned} \quad (11)$$

where  $\beta = 1/k_B T$ ,  $\mu_c(T)$  is the chemical potential determined for fixed electron density  $n_{1D}$  and  $T$ , and

$$F = \sum_{j,\gamma} C_{j,\gamma} f_0[E_j(k_\gamma)]. \quad (12)$$

In deriving Eq. (11), the energy integration over the range  $0 < k < \infty$  is divided into the sum of the integrations between the successive extremum points  $E_j(k_\gamma)$  for  $\gamma=1, 2, \dots$ . For each region,  $E_j(k)$  is a monotonic function of  $k$  with a fixed sign for the group velocity  $v_j(k) = \hbar^{-1} dE_j(k)/dk = -v_j(-k)$ . The quantity  $E_j(k_\gamma)$  is the extremum energy and the last extremum point is a minimum point. For a given curve  $E_j(k)$ ,  $C_{j,\gamma}=1$  for a local energy minimum point and  $C_{j,\gamma}=-1$  for a local energy maximum point. The quantity  $F$  in Eq. (12)

reduces to the total number of pairs of Fermi points at  $T=0$  and is related to the quantized conductance  $G$  by  $G=(2e^2/h)F$ . The result in Eq. (11) is equivalent to the earlier result obtained for the SQWR with a single minimum point for each energy-dispersion curve.<sup>19</sup> It can also be derived using an energy-dependent transmission-coefficient approach.<sup>19,38,39</sup>

The orbital magnetization (in unit of  $\mu_B^*$ ) of electrons at  $T=0$ K is obtained from<sup>28,29</sup>

$$M_\nu(B_x, B_y) = -\frac{1}{\mu_B^*} \left( \frac{\partial u_{\text{av}}}{\partial B_\nu} \right)_{N_e}, \quad (13)$$

where  $\nu=x$  or  $y$ ,  $N_e$  refers to the total number of electrons in the system, and  $(\partial u_{\text{av}}/\partial B_\nu)_{N_e}$  represents the derivative of  $u_{\text{av}}$  with respect to the field component  $B_\nu$  when  $N_e$  is remained unchanged. In Eq. (13),  $\mu_B^*=e\hbar/2m^*$  is the effective Bohr magneton and  $u_{\text{av}}$  is the average energy per electron at  $T=0$  K, given by

$$u_{\text{av}} = \frac{2}{\pi N_e} \sum_j \int_0^\infty dk E_j(k) \theta[E_F - E_j(k)]. \quad (14)$$

Here,  $E_F=\mu_c(0)$  is the Fermi energy at  $T=0$  K.  $M_\nu(B_x, B_y)$  in Eq. (13) depends on both the magnitude and orientation of  $\mathbf{B}$ . The  $B_y$  dependence discussed in this paper refers to the interwire tunnel coupling between  $n \neq n'$  transverse sublevels and is different from the coupling of two orthogonal harmonic oscillators.<sup>30,31</sup>

### III. NUMERICAL RESULTS AND DISCUSSIONS

In our numerical calculations below, we first study the electron sublevel dispersions for various values of  $B_y$  with fixed  $B_x$  as a function of  $k$ , as well as sublevel edges for  $B_x=0$  (i.e., along the wires) as a function of  $B_y$ . Both the lowest-order and the first-order approximations for interwire tunnel coupling are obtained and discussed. From these two approximations, the physics involved in the tunneling modulation, oscillations of the effective tunneling integral with alternating signs, quenching of tunneling, and sublevel repulsion are elucidated. We then investigate the field dependence of the quantized magnetoconductance  $G$ , ballistic electron-diffusion thermoelectric power  $S_d$  at low temperatures, and orbital magnetization  $\mathbf{M}$  as functions of  $B$ . The contour plots for  $G(B_x, B_y)$  and  $S_d(B_x, B_y)$  are presented to provide direct visualizations of their overall anisotropic  $B$  dependence. The parameters for the lower-density sample 1 employed in our numerical calculations are listed in Table I. The parameters for the higher-density sample 2 are the same as those of sample 1 except for  $n_{1D}=2 \times 10^6 \text{ cm}^{-1}$ . For these two samples, we use the electron effective masses  $m^*=0.067m_0$  with  $m_0$  being the free-electron mass. In the following calculations, only the ground tunnel-split doublet is assumed to be populated.

#### A. Wave number and magnetic-field dispersions

Figure 2 displays the sublevel dispersions  $E_j(k)$  at  $B_x=8$  T obtained by diagonalizing Eq. (9) with  $2N_t=40$  for

TABLE I. Double quantum wires (sample 1) with barrier height of 280 meV, well widths  $L_{z_1}/L_{z_2}$ , center-barrier thickness  $L_B$ , ground-doublet tunnel splitting  $\Delta_{\text{SAS}}$  at  $B=0$ , the uniform transverse-sublevel separation  $\hbar\omega_x$ , and linear electron density  $n_{1D}$ . The center-to-center distance  $d$  between two wells is taken to be  $d=(L_{z_1}+L_{z_2})/2+L_B$ .

$L_{z_1}/L_{z_2}$ ( $\text{\AA}$ )	$L_B$ ( $\text{\AA}$ )	$\Delta_{\text{SAS}}$ (meV)	$\hbar\omega_x$ (meV)	$n_{1D}$ ( $10^5 \text{ cm}^{-1}$ )
80	50	1.56	0.2	4

several values of  $B_y$ . In order to highlight the tunnel-induced as well as  $B_y$ -induced anticrossing between  $n \neq n'$  sublevels, we take large  $\hbar\omega_x=1$  meV. Here, we only display lower-energy transverse sublevels for each branch of the tunnel-split doublet. As shown in Fig. 2(a), when  $B_y=0$ , we only see the interwire tunnel coupling between  $n=n'$  sublevels, leading to a ground ( $n=0$ ) tunnel-split doublet with a tunneling gap  $\Delta_{\text{SAS}}$  (indicated by two arrows) at  $k=0$  for  $B_x=8$  T.<sup>14,21</sup> In addition, there exist many equally spaced higher-energy replicas ( $n=1, 2, 3, \dots$ ) of the ground tunnel-split doublet. The Lorentz force due to  $B_x$  and the tunneling motion introduces a relative  $k$  space displacement (proportional to  $B_x$ ) to parabolas of two quantum wires. The degeneracy is lifted at the intersecting point by interwire tunneling and the curves near this point are deformed for large  $B_x$  by the anticrossing gaps between the upper (minimum and electronlike) and lower (maximum and holelike) gap edges, as shown in Fig. 2(a). For  $B_y=4$  T, we find the interwire tunnel coupling between  $n \neq n'$  sublevels, as shown in Fig. 2(b). As a result, each sublevel in the left (right) parabola experiences successive anticrossings with sublevels in the right (left) parabola at higher and higher  $|k|$  values. When  $B_y$  is further increased to 8 T in Fig. 2(c), the interwire tunnel coupling as well as the anticrossing between both  $n=n'$  and  $n \neq n'$  sublevels are quenched for several lower sublevels, leaving many diamond shapes seen in Fig. 2(c).

The tunneling motion of electrons from one wire to another is deflected by the transverse Lorentz force due to  $B_y$ . As a result, the electrons acquire an additional transverse momentum in the final tunneling state along the  $x$  direction. This additional momentum  $\hbar\Delta q = -\hbar d/\ell_{\text{cy}}^2$  directly contributes to a relative phase factor  $\exp[i\Delta qx]$  in Eq. (7) for the wave function in the  $xy$  plane. For  $B_x=0$ , the minimum of each sublevel is always at  $k=0$  for all  $B_y$ . In order to highlight the effect of the  $B_y$ -induced tunneling modulation of the electron energy, we present in Fig. 3 the sublevel edges  $E_j(0)$  (black curves) as a function of  $B_y$  with  $B_x=0$  for the lower-density sample 1. From this figure, we see a very complicated oscillating pattern, resulting from the facts that the effective interwire tunneling gap oscillates with  $B_y$  (tunneling modulation), passes through zero at certain values of  $B_y$ , and becomes negligible at very large  $B_y$  (quenching of tunneling). Moreover, we find the sublevel repulsion, i.e., parallelogram-type shapes, in this figure.  $E_F$  (red curve) in the figure also oscillates with  $B_y$  with kinks (indicated by blue circles) corresponding to sublevel populations or depopulations. Because of sublevel repulsion,  $E_3(0)$  (thick

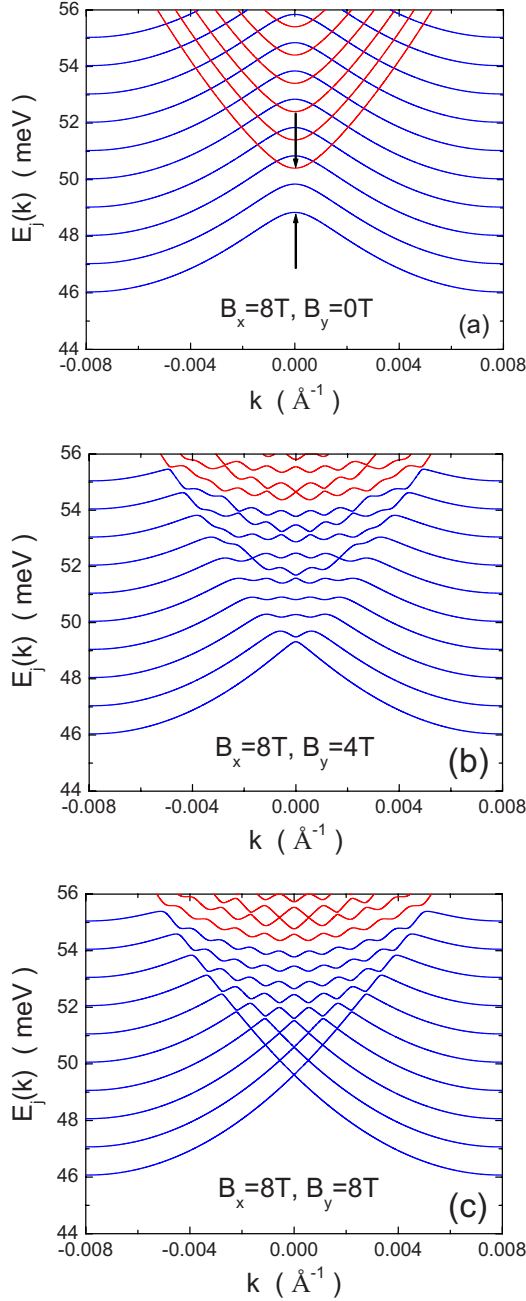


FIG. 2. (Color online) (a)  $E_j(k)$  with  $B_x=8$  T as functions of  $k$  for  $B_y=0$ , (b)  $B_y=4$  T and (c)  $B_y=8$  T. Here, we only display lower-energy transverse sublevels. In (a), the tunnel-split upper (lower) branches in the absence of intersublevel tunneling between  $n \neq n'$  are denoted by red (blue) curves and the anticrossing gaps at  $k=0$  between the upper and lower gap edges are indicated by black arrows for the lowest tunnel-split doublet. In (b) and (c), the higher (lower) coupled sublevels in the presence of intersublevel tunneling between  $n \neq n'$  are represented by red (blue) curves. In our calculations here, we take a large transverse-sublevel separation  $\hbar\omega_x = 1$  meV for a strong confinement in the  $x$  direction.

black curve) initially decreases with  $B_y$  and  $E_3(k)$  is populated near  $k=0$ . This directly leads to the decrease of  $E_F$  with  $B_y$  for  $B_y \leq 0.3$  T. When  $B_y$  is increased above 0.3 T but still small,  $E_3(0)$  begins to increase with  $B_y$  after passing through

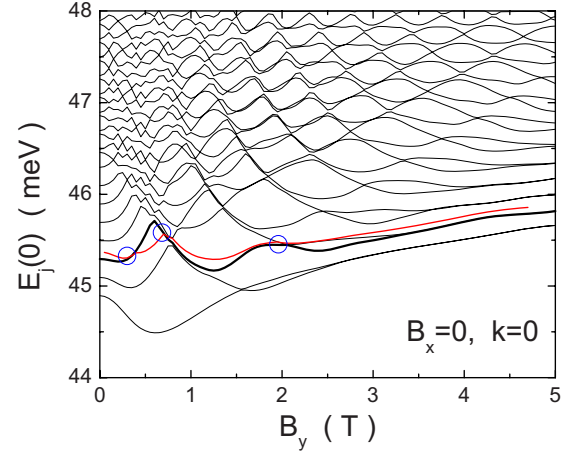


FIG. 3. (Color online)  $E_j(0)$  (black curves) as a function of  $B_y$  for  $B_x=0$ . The red curve represents  $E_F$  of the lower-density sample 1. The sublevel population and depopulation are indicated by three blue circles. The  $E_3(0)$  is displayed by a thick black curve in the figure.

its minimum due to the effect of tunneling modulation. This causes the depopulation of the sublevel  $E_3(k)$  and a kink in  $E_F$  at  $B_y \approx 0.3$  T by transferring electrons from  $E_3(k)$  to  $E_2(k)$ . When  $B_y$  is further increased above 0.6 T but not large,  $E_3(0)$  switches to decrease with  $B_y$  for the same reason of tunneling modulation after passing through its maximum. Consequently, electrons on  $E_2(k)$  are transferred back to  $E_3(k)$ , leading to the recovery of  $E_3(k)$  population and the second significant kink in  $E_F$  at  $B_y \approx 0.7$  T. When  $B_y$  becomes even larger above 0.7 T,  $E_1(0)$  begins to rise after passing through its minimum at  $B_y \approx 0.6$  T. At the same time,  $E_4(0)$  drops after passing through its maximum at  $B_y \approx 1.3$  T, leading to the population of  $E_4(k)$  and a weak kink in  $E_F$  at  $B_y \approx 2$  T. Finally, electron tunneling is quenched for lower sublevels when  $B_y$  is very large and the wires become decoupled, leading to a twofold degeneracy for lower sublevels. This occurs around  $B_y=4.5$  T for the lower five sublevels. The decoupling eventually pins  $E_F$  between  $n=1$  and  $n=2$  sublevels of individual quantum wire.

In order to fully understand these effects, we look into some approximate analytic expressions. For the lowest-order approximation, i.e., only the interwire tunnel coupling between the same sublevels ( $m=0$ ) is considered, we find for  $B_x=0$ ,

$$E_n^{(\pm)}(0) = \left( n + \frac{1}{2} \right) \hbar\omega_x + E_1^z \pm \frac{1}{2} \Delta_{\text{SAS}} e^{-\phi_B^2/4} L_n^{(0)} \left( \frac{\phi_B^2}{2} \right), \quad (15)$$

where  $n=0, 1, 2, \dots$  and  $E_1^z$  is the edge of the ground subband of a single quantum well ( $L_B \rightarrow \infty$ ) at  $B=0$ . The tunnel splitting (last term with  $\pm$  sign) in Eq. (15) oscillates with  $\phi_B$  or  $B_y$  due to  $L_n^{(0)}(\phi_B^2/2)$ . When  $\phi_B^2/2$  becomes one of the roots of  $L_n^{(0)}(x)$ , the tunneling gap shrinks to zero and the  $m=0$  tunnel coupling between two wires passes through zero. Moreover, when  $\phi_B \gg 1$ , the  $m=0$  tunnel coupling is

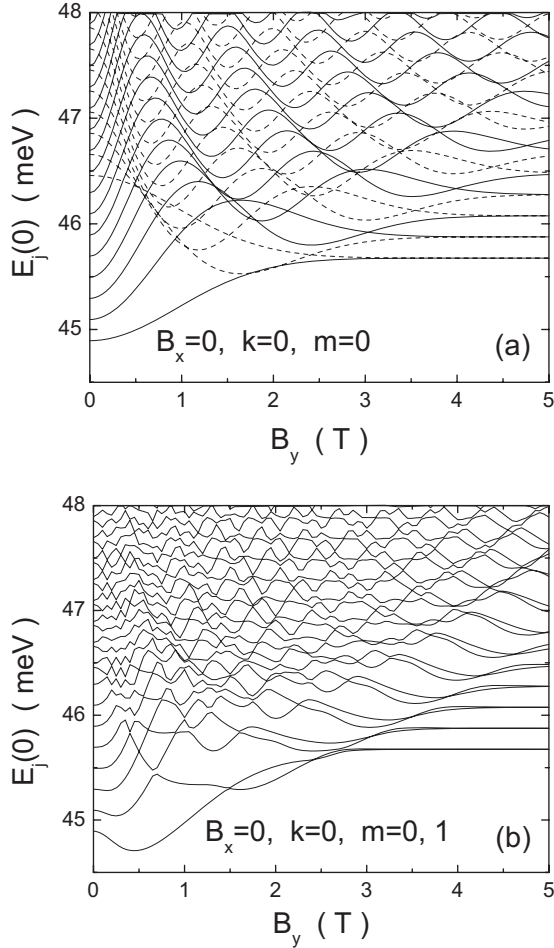


FIG. 4.  $E_j(0)$  as a function of  $B_y$  for  $B_x=0$ . In (a), only the interwire tunnel coupling between  $n=n'$  sublevels ( $m=0$ ) is included in the calculation. In (b), the interwire tunnel coupling between the same sublevels and the nearest-neighboring sublevels ( $m=0, 1$ ) is included in the calculation. The solid and dashed curves in (a) correspond to the sublevel edges  $E_n^{(-)}(0)$  and  $E_n^{(+)}(0)$  in Eq. (15), respectively, with different quantum numbers  $n=0, 1, 2, 3, \dots$

quenched by the exponential factor  $\exp(-\phi_B^2/4)$  in Eq. (15), giving rise to a constant  $E_j(0)$  as a function of  $B_y$ . As a result, the splitting between sublevels  $E_n^{(+)}(k)$  (dashed curves) and  $E_n^{(-)}(k)$  (solid curves) vanishes in Fig. 4(a), forming a degenerated sublevel for a SQWR. All of these described features are clearly demonstrated by Fig. 4(a) with  $m=0$ .

To study the sublevel repulsion, we go beyond the lowest-order approximation in Eq. (15). Under the first-order approximation, we include the interwire tunnel coupling between the nearest-neighboring sublevels with  $m=0, 1$ . The numerical results of  $E_j(0)$  as a function of  $B_y$  are shown in Fig. 4(b) for  $B_x=0$  with  $m=0, 1$ , where we easily find similarities between Figs. 4(a) and 4(b). However, besides these similarities, we also find a self-avoiding feature in Fig. 4(b) for each of intersecting points of sublevels in Fig. 4(a). More important, there is an initial negative  $B_y$  dispersion developed for the first three sublevels close to  $B_y=0$  resulting from the sublevel repulsion. As an example, for the ground sublevel  $E_0^{(-)}(0)$ , we obtain for  $B_x=0$ ,

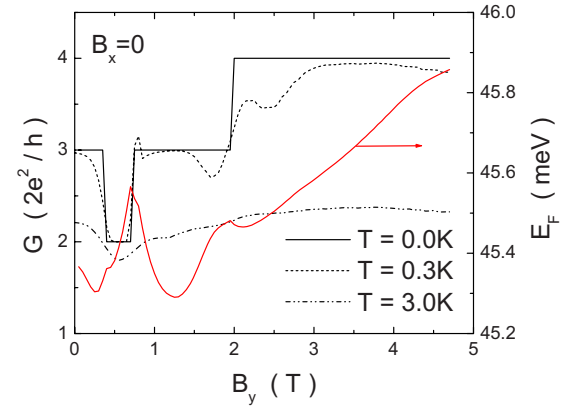


FIG. 5. (Color online)  $G$  (left axis) of the lower-density sample 1 as a function of  $B_y$  for  $B_x=0$  at  $T=0$  K (solid curve), 0.3 K (dashed curve), and 3 K (dash-dot-dotted curve). For the sake of comparison,  $E_F$  (red curve and right axis) is also shown.

$$E_0^{(-)}(0) = E_1^z + \frac{1}{2}\hbar\omega_x - \frac{1}{2}\Delta_{\text{SAS}}e^{-\phi_B^2/4} - \frac{1}{8}\Delta_{\text{SAS}}^2\phi_B^2e^{-\phi_B^2/2} \times \frac{[L_0^{(1)}(\phi_B^2/2)]^2}{\hbar\omega_x + \Delta_{\text{SAS}} \exp(-\phi_B^2/4)[1 - L_1^{(0)}(\phi_B^2/2)]/2}. \quad (16)$$

In Eq. (16), the third term, which is related to the interwire tunnel coupling between  $n=n'$  sublevel, pushes the electron energy up with increasing  $B_y$ , and leads to a positive  $B_y$  dispersion. However, the last term, which is associated with the interwire tunnel coupling between  $n \neq n'$  sublevels, represents the effect of sublevel repulsion and pushes down the ground sublevel with increasing  $B_y$ , leading to a dominant negative  $B_y$  dispersion when  $\phi_B$  is small but nonzero. From Fig. 4(b), we see clearly that the effect of sublevel repulsion greatly modifies the results of the lowest-order approximation in Fig. 4(a) and empowers the first-order approximate calculation approaching the exact solution in Fig. 3. However, the parallelogram-type shapes seen in Fig. 3 are only reproduced for a few of lower sublevels at large values of  $B_y$  in Fig. 4(b) since we have neglected the tunnel coupling for  $m \geq 2$ . The analytical results in Eqs. (15) and (16) with  $m=0, 1$  apply only to the case with a small  $\phi_B$  (or a small  $B_y$ ).

## B. Quantized conductance

Now, we turn to the discussions of numerical results on the field dependence of quantized magnetoconductance  $G$  calculated from Eq. (10). We first demonstrate the effects of  $B_y$  for  $B_x=0$ , as well as the thermal effects on  $G$  by taking various electron temperatures  $T$ . Then, the contour plot of  $G(B_x, B_y)$  is presented to provide a direct visualization for its overall anisotropic  $B$  dependence. Finally, we present  $G$  as a function of  $B_x$  for a set of fixed values of  $B_y$ .

We display in Fig. 5 the thermal effect<sup>1</sup> on  $G$  (left axis) at  $T=0$  K (solid curve), 0.3 K (dashed curve), and 3 K (dash-dot-dotted curve) for the lower-density sample 1 as a function of  $B_y$  for  $B_x=0$ . The features on  $E_F$  (red curve and right

axis) in this figure have already been explained in detail in Fig. 3 and are used here as a guidance. Compared with Fig. 3, we find for  $T=0$  K that the first downward step of  $G$  at  $B_y \approx 0.3$  T results from the depopulation of  $E_3(k)$ , while the successive first and second upward steps of  $G$  are associated with the populations of  $E_3(k)$  and  $E_4(k)$  at  $B_y \approx 0.7$  T and 2 T, respectively. The constant  $G$  for  $B_y \geq 2$  T is a result of the pinning of  $E_F$  between  $n=1$  and  $n=2$  sublevels in decoupled wires. We also see that when  $T$  is raised to 3 K, all the  $G$  steps at  $T=0$  K, which are related to population (depopulation) of sublevels, are completely washed out except for a minimum at  $B_y \approx 0.5$  T (dash-dot-dotted curve) after a thermal average is performed to the total number of pairs of Fermi points  $N_F(E)$  within the energy range  $[\mu_c - k_B T, \mu_c + k_B T]$  to get  $\mathcal{N}(\mu_c)$  in Eq. (10). Moreover,  $G$  at  $T=3$  K is greatly reduced compared to that at  $T=0$  K due to the decreased  $\mathcal{N}(\mu_c)$  by reduction of the chemical potential  $\mu_c(T)$  with increasing  $T$  ( $d\mu_c/dT < 0$ ) from 0 to 3 K. When  $T=0.3$  K, the sharp corner of the upward (downward) step (dashed curve) is rounded off, and there is always a dip right after the peak for each upward step.

In Fig. 6(a), we present the contour plot of  $G(B_x, B_y)$  for the higher-density sample 2 to display its overall anisotropic  $B$  dependence. The  $B_y$  evolution is best visualized from Fig. 6(a) by a vertical narrow slit scanning for successive increasing values of  $B_y$ . The yellow and orange regions in this contour plot represent the “mountains” for higher values of  $G(B_x, B_y)$  when  $B_x \geq 6$  T, while the purple (blue) regions represent the “valleys” for lower values of  $G(B_x, B_y)$  when  $B_y \leq 4$  T. In addition, the green (cyan) regions correspond to the “plains” for intermediate values of  $G(B_x, B_y)$ . In order to explain the physics involved in the anisotropic  $B$  dependence of  $G(B_x, B_y)$  in Fig. 6(a), we display  $G$  in Fig. 6(b) for the same sample as a function of  $B_x$  for a set of fixed values of  $B_y$ .  $G$  in Fig. 6(b) starts with a deep V shape<sup>36</sup> for  $B_y=0$  (bottom black curve), evolving to a nearly constant as a function of  $B_x$  except for two major downward spikes when  $B_y=7$  T (top orange curve). For this V-shaped  $G$  at  $B_y=0$ , each downward step corresponds to a depopulation of one sublevel in upper tunnel-split branches (one pair of Fermi points to none), while each upward step corresponds to a depopulation of one lower gap edge (LGE) point at  $k=0$  in lower tunnel-split branches (one pair of Fermi points to two pairs). When  $B_x$  is small, the relative displacement of the parabolas of two wires in  $k$  space is too small to form any LGE points at  $k=0$ . When  $B_x$  is large, on the other hand, the energy of the LGE points at  $k=0$  is so high that two wires become decoupled. The flat  $G$  for large values of  $B_x$ , i.e., the orange region in Fig. 6(a), is associated with the rise of the lowest LGE point above the Fermi energy. The degradation of V shape with increasing  $B_y$  in Fig. 6(b) indicates the close of anticrossing gaps at some lower energy LGE points and the increased energy of the lowest crossing point at  $k=0$  for large  $B_y$ , as shown in Fig. 2(c).

### C. Ballistic electron-diffusion thermoelectric power

In this subsection, we discuss the field dependence of the ballistic electron-diffusion thermoelectric power  $S_d$  calcu-

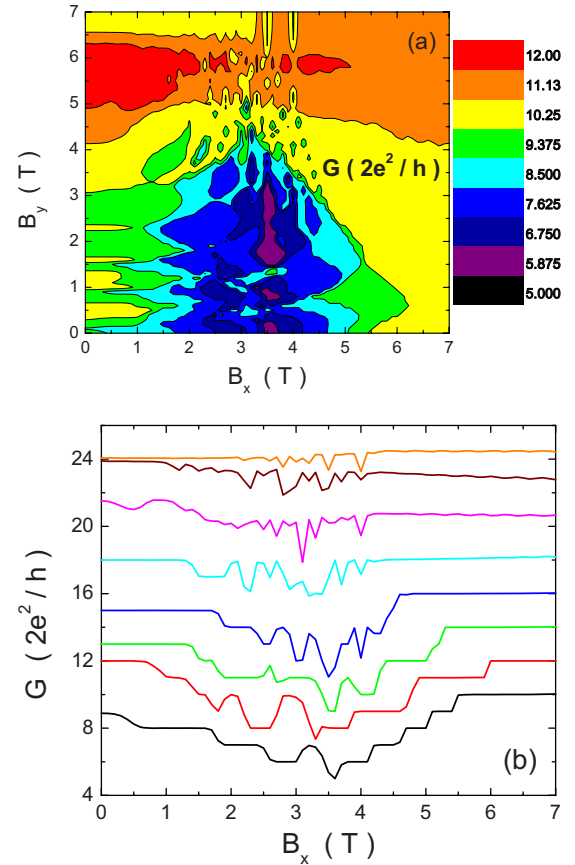


FIG. 6. (Color online) Contour plot of  $G(B_x, B_y)$  in (a) and  $G$  in (b) as a function of  $B_x$  with a set of fixed values of  $B_y$  for the higher-density sample 2. We set  $T=0$  K for our calculations here. For the sake of clarity, the successive curves from the bottom black curve in (b) are vertically shifted by an amount of  $2(2e^2/h)$ . The curves from the bottom to the top in (b) correspond to  $B_y = 0, 1, 2, \dots, 7$  T, respectively.

lated from Eqs. (11) and (12). First, we find the correspondence between the peaks of  $S_d$  and the steps of  $G$  at low temperatures. We then present the contour plot of  $S_d(B_x, B_y)$  to provide a complete visualization for its complicated anisotropic field dependence. Finally, we present  $S_d$  as a function of  $B_x$  for a set of fixed values of  $B_y$ .

In Fig. 7(a), we display a blown-up view of the sublevel edges  $E_j(0)$  (black curves) close to  $E_F$  (red curve) for the higher-density sample 2 as a function of  $B_y$ . The sublevel populations (depopulations) are clearly seen. These sublevel populations and depopulations are directly reflected in the upward and downward steps in  $G$  (left axis and dashed curve) in Fig. 7(b) for the same sample. Two upward sharp peaks at  $B_y=1.5$  and 2.2 T (indicated by two blue arrows) result from successive population-depopulation processes close to the two sharp minima of sublevel edges [indicated by blue circles in (a)] induced by tunneling modulation. In addition,  $G$  becomes independent of  $B_y$ , once the interwire tunneling is quenched at  $B_y \geq 7$  T. For  $k_B T / \hbar \omega_x = 0.02$ ,  $S_d < 0$  (right axis and solid curve) in Fig. 7(b) shows a series of upward sharp peaks superposed on the  $S_d=0$  background when  $B_y \leq 4$  T. However, as  $B_y > 4$  T, the interwire tunnel

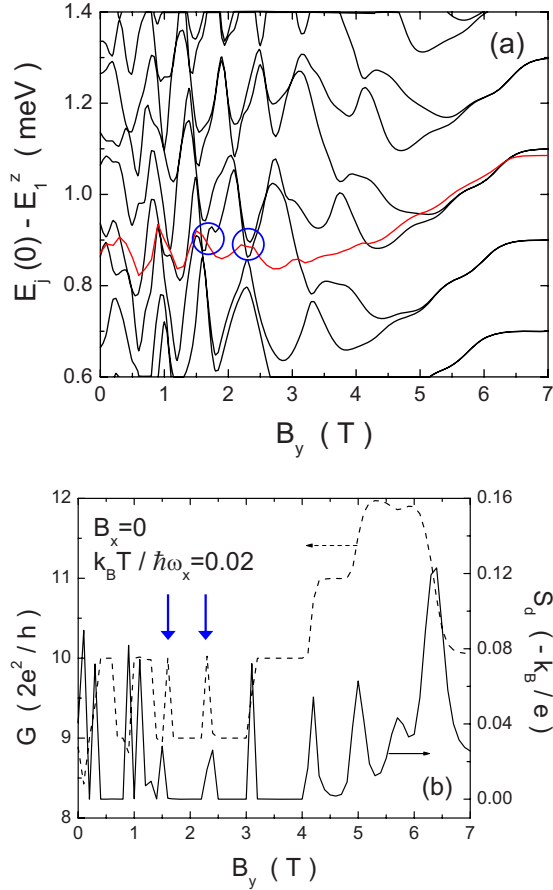


FIG. 7. (Color online) Blown-up view for  $E_j(0) - E_1^z$  (black curves) close to  $E_F$  in (a) as a function of  $B_y$  and  $S_d$  (right axis and solid curve) in (b) as a function of  $B_y$  for the higher-density sample 2. For the sake of comparison,  $E_F$  (red curve) in (a) as well as  $G$  (dashed curve) in (b) are also shown. Here,  $S_d < 0$  (in unit of  $-k_B/e$ ) for electrons in the wires. The successive population (depopulation) of two sharp minima in (a) are indicated by blue circles. Two corresponding sharp peaks in  $G$  are indicated by blue vertical arrows.

coupling is gradually reduced, leading to an increasing  $S_d$  background with  $B_y$ . Each peak of  $S_d$  corresponds to a jump in  $G$  at the same value of  $B_y$ . Two sharp peaks of  $G$  only lead to two relatively weak peaks in  $S_d$  because  $S_d$  is inversely proportional to  $G$ .

In Fig. 8(a), we present the contour plot of  $S_d(B_x, B_y)$  at  $k_B T / \hbar \omega_x = 0.02$  for the higher-density sample 2 in order to demonstrate its overall anisotropic  $B$  dependence. The  $B_y$  evolution is very well observed from Fig. 8(a) by taking a snapshot through a narrow slit moving upward for each successive increasing value of  $B_y$ . The yellow region in this contour plot represents the “mountain range” for higher positive values of  $-S_d(B_x, B_y)$  when  $B_y \geq 5$  T, while the green (cyan) regions represent the “lands” for lower positive values of  $-S_d(B_x, B_y)$  when  $B_y \leq 5$  T. Furthermore, the isolated blue (purple) regions correspond to the “lakes” for negative values of  $-S_d(B_x, B_y)$ . The blue (purple) lakes mostly exist for  $3 \leq B_y \leq 5$  T and  $2 \leq B_x \leq 5$  T, while the yellow mountain range is easily found for  $B_x \geq 4$  T within the range of  $5 \leq B_y \leq 7$  T. This mountain range expands itself into the re-

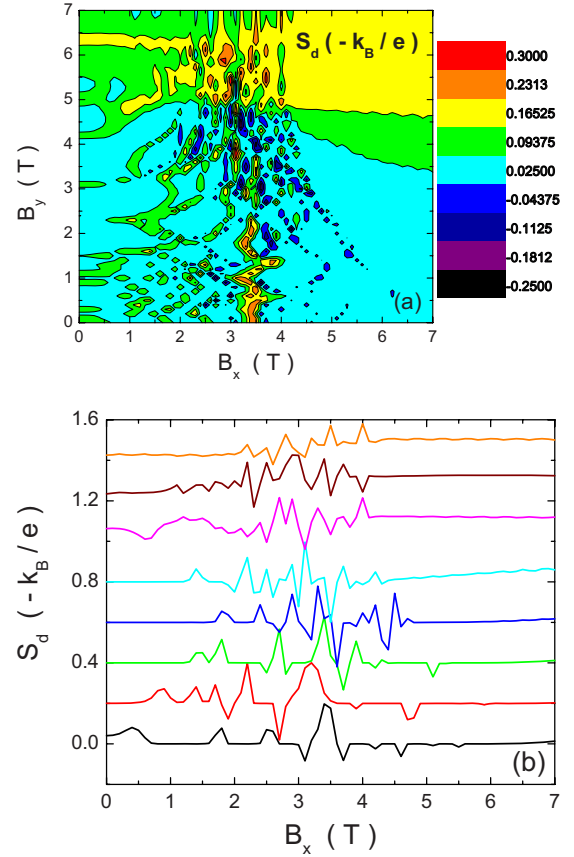


FIG. 8. (Color online) Contour plot of  $S_d(B_x, B_y)$  in (a) and  $S_d$  in (b) as a function of  $B_x$  with a set of fixed values of  $B_y$  for the higher-density sample 2. We set  $k_B T / \hbar \omega_x = 0.02$  for our calculations here. For the sake of clarity, the successive curves from the bottom black curve in (b) are vertically shifted by an amount of  $0.2(-k_B/e)$ . The curves from the bottom to the top in (b) are associated with  $B_y = 0, 1, 2, \dots, 7$  T, respectively.

gion of  $B_x < 4$  T with many “mountain peaks” (unconnected yellow regions) for  $5 \leq B_y \leq 7$  T. In order to explain the physics involved in the anisotropic  $B$  dependence of  $S_d(B_x, B_y)$  in Fig. 8(a), we display  $S_d$  in Fig. 8(b) for the same sample as a function of  $B_x$  for a set of fixed values of  $B_y$ .  $-S_d$  in Fig. 8(b) starts with one dominant peak for  $B_y = 0$  with positive (negative) peaks on the left (right) side of it (bottom black curve), evolving into multiple peaks sandwiched by lower (higher) plateaus on the left (right) side for  $B_y = 7$  T (top orange curve). For  $B_y = 0$ , whenever a sublevel in upper tunnel-split branches is depopulated,  $-S_d$  displays a positive peak (minimum) is electronlike. On the other hand,  $-S_d$  displays a negative peak whenever a LGE point in lower tunnel-split branches is depopulated since the dispersion for a LGE point (maximum) is holelike. The positive peak of  $-S_d$  near the minimum of  $G$  at  $B_x = 3.4$  T is large because  $S_d$  is inversely proportional to  $G$ . For large  $B_y$ , the peaks and dips of  $S_d$  occur only for intermediate values of  $B_x$ , in which there exist many LGE points with significant anticrossing gaps below and above the Fermi energy. The flat  $S_d$  for large values of  $B_x$ , i.e., the yellow region in Fig. 8(a), corresponds to the rise

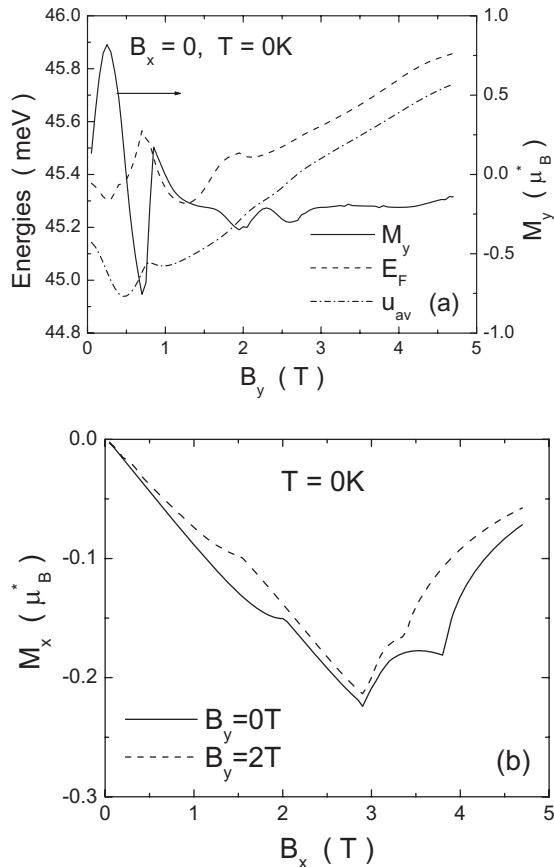


FIG. 9.  $M_y$  (right axis and solid curve) as a function of  $B_y$  for  $B_x=0$  in (a) and  $M_x$  as a function of  $B_x$  in (b) with  $B_y=0$  (solid curve) and  $B_y=2$  T (dashed curve) for the lower-density sample 1. For comparison,  $E_F$  (left axis and dashed curve) and the average energy per electron  $u_{av}$  (left axis and dash-dotted curve) are also shown in (a).

of the lowest LGE point above the Fermi energy in decoupled wires.

#### D. Orbital magnetization

In this subsection, we briefly discuss the numerical results on orbital magnetization calculated according to Eqs. (13) and (14). We present in Fig. 9  $M_y$  as a function of  $B_y$  for  $B_x=0$  [in (a)] and  $M_x$  as a function of  $B_x$  for  $B_y=0$  and 2 T [in (b)] for the lower-density sample 1 at  $T=0$  K. As explained in Fig. 3,  $E_F$  (left axis and dashed curve) decreases with  $B_y$  initially for small  $B_y$  in Fig. 9(a) due to the sublevel repulsion, oscillates with  $B_y$  due to the tunneling modulation, and then produces few kinks at the same time due to the population or depopulation of sublevels. For large  $B_y$ , all the sublevel edges  $E_j(0)$  eventually become independent of  $B_y$  [e.g., see Fig. 7(a)], giving rise to a  $B_y$ -independent  $E_F$ . From Fig. 9(a), we find that the average energy per electron  $u_{av}$  (left axis and dash-dotted curve) follows  $E_F$  accordingly. Therefore,  $u_{av}$  oscillates with small  $B_y$ , becomes nearly proportional to  $B_y$  due to pinning of  $E_F$  when  $3 \leq B_y \leq 5$  T, and approaches a constant when  $B_y \geq 6$  T (not shown). Consequently, a profound oscillation in  $M_y$  (right axis and solid

curve) is observed for small  $B_y$  with a sign change, followed by a small negative and nearly constant  $M_y$  for large  $B_y$ , and eventually approaches zero for  $B_y \geq 6$  T. For  $M_x$  as a function of  $B_x$  in Fig. 9(b), we see a V-shaped  $M_x < 0$ . For  $B_y = 0$  (solid curve), the initial linear drop of  $M_x$  within the range of  $0 \leq B_x < 2$  T is associated with the diamagnetic shift of sublevels with  $B_x$ . For  $2 \leq B_x < 3$  T,  $M_x$  continuously decreases with  $B_x$  after passing the kink at  $B_x = 2$  T due to depopulation of a sublevel edge from the upper tunnel-split branches. For  $3 \leq B_x < 4$  T,  $M_x$  begins to increase with  $B_x$  with two kinks at  $B_x = 3$  T and 4 T, respectively, due to the depopulation of two LGE points from the lower tunnel-split branches. Finally,  $M_x$  increasingly approaches zero as  $B_x > 4$  T. As  $B_y$  is increased from zero to 2 T (dashed curve), the depopulations of the sublevel edge and the second LGE point shift down from  $B_x = 2$  to 1.5 T and from  $B_x = 4$  to 3.5 T, respectively. In addition,  $M_x$  approaches zero with small  $B_x$  after the last LGE point is depopulated at  $B_x = 3.5$  T.

#### IV. CONCLUSIONS

In conclusion, we have studied the effect of the modulation of interwire tunneling due to a parallel magnetic field  $B_y$  along the wire on the ballistic conductance, the thermoelectric power, and the orbital magnetization in the presence of a perpendicular field component  $B_x$ . The parallel component  $B_y$  introduces tunnel coupling between the sublevels  $n \neq n'$  of the two wires and modifies tunneling between  $n = n'$  sublevels, resulting in oscillations of the effective tunneling integral with alternating signs and quenching of tunneling for large  $B_y$ . The role of  $B_x$  is to displace the tunnel-free energy-dispersion curves associated with each of the wires relative to each other in  $k$  space. The physics of the effect of the interplay between  $B_x$  and  $B_y$  on the field-induced distortion of the crossing and the anticrossing between the sublevels of the wires was explored.

The anisotropic  $B$  dependence of the quantized  $G$  has been fully demonstrated by its contour plot. For  $B_y = 0$ , we see a V-shaped  $G$  as a function of  $B_x$ . In this case, the downward and upward steps are related to the depopulations of sublevel edges in the upper tunnel-split branches and the depopulations of LGE points in the lower tunnel-split branches. For high  $B_y$ , on the other hand, we find a nearly constant  $G$  as a function of  $B_x$  except for two major downward spikes. In this case, the interwire tunnel coupling is quenched and two quantum wires become decoupled.

The anisotropic  $B$  dependence of  $S_d$  has also been displayed by using a contour plot. For  $B_y = 0$ , we find one dominant peak in  $S_d$  sandwiched by positive and negative peaks on both sides. In this case, the positive peaks on the lower- $B_x$  side come from the depopulations of sublevel edges (electronlike) in the upper tunnel-split branches, while the negative peaks on the higher- $B_x$  side come from the depopulations of LGE points (holelike) in the lower tunnel-split branches. For high  $B_y$ , on the other hand, we find multiple peaks in  $S_d$  sandwiched by lower and higher plateaus on the lower- and higher- $B_x$  sides, respectively. In this case, the interwire electron tunnel coupling between  $n \neq n'$  sublevels is quenched.

The  $B$  dependence of  $\mathbf{M}$  at  $T=0$  K has been studied. For  $B$  along the wires, we have found that the  $B_y$  dependence of  $u_{av}$  follows closely the change of  $E_F$ : with increasing  $B_y$ , it decreases initially due to the sublevel repulsion, oscillates due to the tunneling modulation, and changes linearly with  $B_y$  due to the pinning of  $E_F$ , eventually becoming independent of  $B_y$  due to the quenching of tunneling. As a result, we find a profound oscillation in  $M_y$  with a sign reversal for small  $B_y$  because of sublevel repulsion. For intermediate  $B_y$ ,  $M_y$  becomes negative and nearly constant and vanishes for large  $B_y$ . For fixed values of  $B_y$ , a V-shaped  $M_x$  is seen as a function of  $B_x$  due to the diamagnetic shift of sublevels, depopulation of sublevel edges, and LGE points.

Through our numerical calculations, we have demonstrated the existence of interwire tunnel coupling between  $n \neq n'$  sublevels by comparing Figs. 2(a) and 2(b) for  $B_y=0$  and 4 T, respectively. With a finite  $B_y$ , each sublevel in the

left (right) parabola goes through successive anticrossings with sublevels in the right (left) parabola. The unique  $k$  dispersion of energy levels has been observed experimentally by Thomas *et al.*, as shown in Figs. 3(a) and 3(b) of Ref. 40. With further increase of  $B_y$ , the quenching of both interwire tunnel coupling and the anticrossing between  $n=n'$  and  $n \neq n'$  sublevels develops gradually, as can be found from Fig. 2(c). This quenching behavior has been observed previously by Thomas *et al.*, as shown in Fig. 2(b) of Ref. 40.

#### ACKNOWLEDGMENTS

Sandia is a multiprogram laboratory operated by Sandia Corporation, a Lockheed Martin Company, for the U.S. DOE under Contract No. DE-AC04-94AL85000. D.H. would like to thank the support from the Air Force Office of Scientific Research (AFOSR).

- 
- <sup>1</sup>S. K. Lyo and D. Huang, Phys. Rev. B **64**, 115320 (2001).  
<sup>2</sup>S. K. Lyo and D. H. Huang, Phys. Rev. B **66**, 155307 (2002).  
<sup>3</sup>S. K. Lyo and D. H. Huang, Phys. Rev. B **68**, 115317 (2003).  
<sup>4</sup>S. K. Lyo and D. H. Huang, J. Phys.: Condens. Matter **16**, 3379 (2004).  
<sup>5</sup>S. K. Lyo and D. H. Huang, Phys. Rev. B **73**, 205336 (2006).  
<sup>6</sup>J. Lee and H. N. Spector, J. Appl. Phys. **54**, 3921 (1983).  
<sup>7</sup>G. Fishman, Phys. Rev. B **34**, 2394 (1986).  
<sup>8</sup>H. Sasaki, T. Noda, K. Hirakawa, M. Tanaka, and T. Matsusue, Appl. Phys. Lett. **51**, 1934 (1987).  
<sup>9</sup>S. Das Sarma and X. C. Xie, Phys. Rev. B **35**, 9875 (1987).  
<sup>10</sup>K. F. Berggren, G. Roos, and H. van Houten, Phys. Rev. B **37**, 10118 (1988).  
<sup>11</sup>H. Akera and T. Ando, Phys. Rev. B **43**, 11676 (1991).  
<sup>12</sup>B. Tanatar and A. Gold, Phys. Rev. B **52**, 1996 (1995).  
<sup>13</sup>J. S. Moon, M. A. Blount, J. A. Simmons, J. R. Wendt, S. K. Lyo, and J. L. Reno, Phys. Rev. B **60**, 11530 (1999).  
<sup>14</sup>A. Kurobe, I. M. Castleton, E. H. Linfield, M. P. Grimshaw, K. M. Brown, D. A. Ritchie, M. Pepper, and G. A. C. Jones, Phys. Rev. B **50**, 4889 (1994).  
<sup>15</sup>C. V. J. Beenaker and H. van Houten, in *Semiconductor Heterostructures and Nanostructures*, Solid State, Physics Vol 44, edited by H. Ehrenreich and D. Turnbull (Academic, New York, 1991), and references therein.  
<sup>16</sup>B. J. van Wees, L. P. Kouwenhoven, H. van Houten, C. W. J. Beenakker, J. E. Mooij, C. T. Foxon, and J. J. Harris, Phys. Rev. B **38**, 3625 (1988).  
<sup>17</sup>K. J. Thomas, J. T. Nicholls, W. R. Tribe, M. Y. Simmons, A. G. Davis, D. A. Ritchie, and M. Pepper, Physica E (Amsterdam) **6**, 581 (2000).  
<sup>18</sup>H. van Houten, L. W. Molenkamp, C. W. J. Beenakker, and C. T. Foxon, Semicond. Sci. Technol. **7**, B215 (1992).  
<sup>19</sup>P. Streda, J. Phys.: Condens. Matter **1**, L1025 (1989).  
<sup>20</sup>M. Tsaousidou and P. N. Butcher, Phys. Rev. B **56**, R10044 (1997).  
<sup>21</sup>S. K. Lyo, Phys. Rev. B **50**, 4965 (1994).  
<sup>22</sup>S. K. Lyo, Phys. Rev. B **60**, 7732 (1999).  
<sup>23</sup>H. L. Störmer, T. Haavasoja, V. Narayaramurti, A. C. Gossard, and W. Wiegmann, J. Vac. Sci. Technol. B **1**, 423 (1983).  
<sup>24</sup>F. F. Fang and P. J. Stiles, Surf. Sci. **142**, 290 (1984).  
<sup>25</sup>T. Haavasoja, H. L. Störmer, D. J. Bishop, V. Narayaramurti, A. C. Gossard, and W. Wiegmann, Surf. Sci. **142**, 294 (1984).  
<sup>26</sup>E. Gornik, R. Lassnig, G. Strasser, H. L. Störmer, A. C. Gossard, and W. Wiegmann, Phys. Rev. Lett. **54**, 1820 (1985).  
<sup>27</sup>J. P. Eisenstein, H. L. Störmer, V. Narayanamurti, A. Y. Cho, A. C. Gossard, and C. W. Tu, Phys. Rev. Lett. **55**, 875 (1985).  
<sup>28</sup>A. H. MacDonald, H. C. A. Oji, and K. L. Liu, Phys. Rev. B **34**, 2681 (1986).  
<sup>29</sup>X. C. Xie, Q. P. Li, and S. Das Sarma, Phys. Rev. B **42**, 7132 (1990).  
<sup>30</sup>G. Marx and R. Kümmel, J. Phys.: Condens. Matter **3**, 8237 (1991).  
<sup>31</sup>G. Ihm, M. L. Falk, S. K. Noh, J. I. Lee, and S. J. Lee, Phys. Rev. B **46**, 15530 (1992).  
<sup>32</sup>S. K. Lyo and D. H. Huang, Curr. Appl. Phys. **4**, 491 (2004).  
<sup>33</sup>S. F. Fischer, G. Apetrii, U. Kunze, D. Schuh, and G. Abstreiter, Nat. Phys. **2**, 91 (2006); Phys. Rev. B **74**, 115324 (2006).  
<sup>34</sup>Lev G. Mourokh, A. Yu. Smirnov, and S. F. Fischer, Appl. Phys. Lett. **90**, 132108 (2007).  
<sup>35</sup>S. K. Lyo, J. Phys.: Condens. Matter **8**, L703 (1996).  
<sup>36</sup>S. K. Lyo, Phys. Rev. B **60**, 7732 (1999).  
<sup>37</sup>J. M. Ziman, *Principles of the Theory of Solids*, 2nd ed. (Cambridge University Press, Cambridge, 1999), p. 236.  
<sup>38</sup>R. Landauer, Z. Phys. B: Condens. Matter **68**, 217 (1987).  
<sup>39</sup>M. Büttiker, Phys. Rev. Lett. **57**, 1761 (1986).  
<sup>40</sup>K. J. Thomas, J. T. Nicholls, M. Y. Simmons, W. R. Tribe, A. G. Davies, and M. Pepper, Phys. Rev. B **59**, 12252 (1999).